

# Influence of Ablation on Vacuum-Ultraviolet Radiation in a Plasma Wind Tunnel Flow

Tobias Hermann<sup>a</sup>, Stefan Löhle<sup>b</sup> and Stefanos Fasoulas<sup>c</sup>  
*Universität Stuttgart, Institut für Raumfahrtssysteme,  
Pfaffenwaldring 29, D-70569 Stuttgart, Germany*

Pénélope Leyland<sup>d</sup>,  
*Ecole Polytechnique Fédérale de Lausanne,  
Interdisciplinary Aerodynamics Group, CH-1015 Lausanne, Switzerland*

Lionel Marraffa<sup>e</sup>,  
*ESA/ESTEC, Aerothermodynamics Section, NL-2200 AG Noordwijk, Netherlands*

Jean-Marc Bouilly,  
*Astrium SAS, F-33160 Saint-Médard-en-Jalles, France*

Plasma wind tunnel experiments have been performed simulating a Hayabusa re-entry trajectory point at 78.8 km altitude with a velocity of 11.7 km/s corresponding to a local mass-specific enthalpy of 68.4 MJ/kg and a stagnation pressure of 2.44 kPa. Ablation-radiation coupling is investigated using a carbon preform sample, a lightweight carbon phenolic ablator sample and cooled copper. Optical emission spectroscopic measurements in the vacuum ultraviolet (VUV) regime (116 nm–197 nm) have been conducted through a bore hole in the stagnation point of the different samples. Optical emission spectroscopic measurements in the UV/VIS spectral range (320 nm–810 nm) have been conducted viewing the plasma from the side. The stagnation point VUV radiation to the carbon preform sample is strongest while it is weakest for the carbon phenolic sample. In the UV/VIS both carbon based material sam-

<sup>a</sup> PhD student, High Enthalpy Flow Diagnostic Group, IRS, Member AIAA

<sup>b</sup> Research Scientist, High Enthalpy Flow Diagnostic Group, IRS, Member AIAA

<sup>c</sup> Professor, Director, IRS, Senior Member AIAA

<sup>d</sup> Interdisciplinary Aerodynamics Group, EPFL, Member AIAA

<sup>e</sup> Aerothermodynamics Section, ESA/ESTEC, Member AIAA

ples lead to stronger plasma radiation than copper. Atomic number densities in front of the samples are largest for the carbon preform sample and lowest for the carbon phenolic sample. Rotational and vibrational temperatures are lower for both the carbon based materials compared to copper. The measurements show for the first time experimentally the radiative heat flux mitigation by carbon phenolic materials.

### Nomenclature

$E_i$  = state energy,  $\text{cm}^{-1}$

$f$  = focal length, mm

$g_i$  = state degeneracy

$L_\lambda$  = spectral radiance,  $\text{W}/(\text{m}^2 \text{ nm sr})$

$L$  = radiance,  $\text{W}/(\text{m}^2 \text{ sr})$

$n$  = number density,  $\text{m}^{-3}$

$n_i$  = excited state population density,  $\text{m}^{-3}$

$r$  = radial location, mm

$T$  = temperature, K

$\varepsilon$  = emission coefficient,  $\text{W}/(\text{m}^3 \text{ nm sr})$

$\varepsilon_c$  = wavelength integrated emission coefficient,  $\text{W}/(\text{m}^3 \text{ sr})$

$\lambda$  = wavelength, nm

$\lambda_0$  = central wavelength, nm

### *Subscripts*

e = electron

exc = electronic excitation

rot = rotational

vib = vibrational

## I. Introduction

Re-entry vehicles entering the Earth's atmosphere on hyperbolic trajectories are exposed to very high thermal loads, comprising of a convective and a radiative component. As the re-entry speed **and the free stream density increase**, the radiative part of the heat flux becomes more and more dominant [1–4]. Within the flow field, energy transfer is conducted by radiative transport in addition to convective and diffusive mechanisms [5]. In order to protect the vehicle from these thermal loads, ablative heat shields are used. The introduction of carbonaceous and phenolic species originating from the ablative heat shield can have an effect on all energy transport mechanisms [6–9]. For high radiative heat fluxes the coupling of ablation and radiation needs to be investigated in order to set useful design margins for the thermal protection system. New radiating species originating from the heat shield are introduced, e. g. atomic carbon and cyanogen (CN) increasing the radiative heat flux. However, species from the heat shield can also act as strong absorbers thus reducing the radiative heat flux. Absorbed radiation is either re-emitted or transported downstream becoming an additional convective heat flux to the wall [10]. Both increases and decreases in radiative heating through ablation have been reported in numerical analyses [6, 11, 12]. In terms of total radiative heat flux encountered by the vehicle the vacuum ultraviolet (VUV) regime, i. e. 100 nm–200 nm, is considered the main source [9, 10, 13–16]. However, experimental investigations of this wavelength regime are sparse [17–22]. Considering the lack of experimental investigations and the fact that ablation-radiation coupling is still not sufficiently understood, the need for experimental data on the subject is clear. Experimental data provides the opportunity to validate numerical simulations of such complex physical environments. Furthermore, diagnostic techniques enable the investigation of coupling effects between the material and the thermophysical state of the boundary layer.

In this study the ablation and radiation processes have been investigated in a plasma wind tunnel as this type of ground based facility provides steady-state high enthalpy flow environments representative of re-entry flows [23–27]. A whole suite of optical diagnostic techniques has been employed in order to evaluate the physical parameters driving the radiation and ablation: Spectroscopy in the VUV measuring radiation through a hole in the stagnation point of the sample, spectroscopic measurements in the ultraviolet and visible spectral range (UV/VIS) viewing the plasma from the

side, in-situ recession measurements with photogrammetry, pyrometry and thermography [28, 29]. The combination of the different measurements allows, for the first time, a detailed insight into the coupling of ablation and radiation including the VUV spectral range. This then provides a unique dataset for a numerical rebuilding of the experimental conditions and the material response.

This paper provides an analysis of the VUV and UV/VIS spectroscopic data. The influence of different materials on the local emission coefficient in the UV/VIS, as well as on the measured VUV radiance is studied. Both spectroscopic datasets are used to evaluate emission and self-absorption processes in the flow allowing the determination of absolute particle densities of various species [30]. Different excited states of atoms are used to measure electronic excitation temperatures [31–33]. Molecular radiation is used to determine rotational and vibrational excitation temperatures [15, 34–36]. Using these techniques allows, for the first time, the quantitative study of the influence of ablation on VUV radiation and the thermochemical state of the plasma in front of the material samples.

## II. Experimental setup

Experiments have been conducted in the plasma wind tunnel PWK1. Details of the facility setup for this campaign can be found in [28]. The high-enthalpy air flow is provided by a magnetoplasmadynamic arcjet generator (RD5) [24]. Three different material types are tested: A carbon preform (CALCARB), a lightweight carbon phenolic ablator (ASTERM) and cooled copper. The different samples (diameter 40 mm) are mounted in a probe (diameter 80 mm) on a moving platform inside the vacuum chamber. The probe is moved horizontally inside the chamber to set the specified heat load and total pressure. A photograph of the probe with a sample installed is shown in Fig. 1. CALCARB is used as a reference material without phenolic resin in order to investigate surface effects, e. g. volumetric oxidation, but without the influence of pyrolysis and blowing [37, 38]. The carbon phenolic material (ASTERM) is a lightweight ablator developed by AIRBUS and therefore the only flight candidate material within this study [39]. For comparison to the non-ablating case a cooled copper sample is mounted. However, the surface catalytic properties are probably different from the carbon based materials.

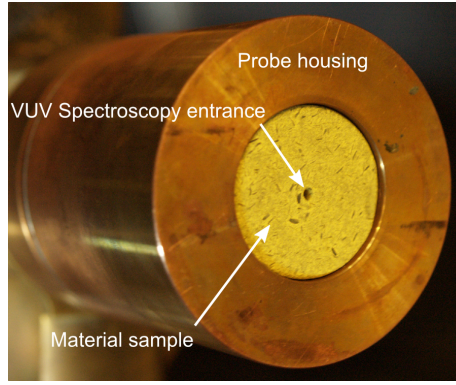


**Fig. 1 Probe with material sample installed.**

#### **A. Flow condition**

The flow condition used in this testing has been realized in the plasma wind tunnel PWK1 at a local mass-specific enthalpy of 68.4 MJ/kg and a stagnation pressure of 2.44 kPa, which corresponds to a Hayabusa re-entry trajectory point at 78.8 km with a velocity of 11.7 km/s [43, 44]. This trajectory point is of particular interest, as it has been observed with optical instruments aboard an aircraft [23, 45]. The corresponding plasma wind tunnel flow condition has also been the target of a previous investigation [30]. The resulting free stream condition has been measured and the flow parameters are summarized in Table 1. Free stream velocity and translational temperature have been measured by Zander et al. [40]. The translational temperature is calculated using mole fraction averaging of the deduced translational temperatures of atomic oxygen and nitrogen respectively. Free stream mole fractions are approximated by applying chemical equilibrium at the measured enthalpy and static pressure condition using the chemical equilibrium with applications (CEA) lookup tables [46]. The material parameters as well as the measured stagnation point recession rates and surface temperatures are summarized in Table 2.

#### **B. VUV spectroscopy**

The VUV spectroscopy, covering the 116 nm–197 nm wavelength region, has been designed to measure through a bore hole in the sample’s stagnation point. The light enters the evacuated probe through a MgF<sub>2</sub> window and is redirected towards the spectrometer on the outside of the vessel. The setup is depicted schematically in Fig. 2. An ACTON RESEARCH CORPORATION VM-521-SG

**Table 1 Stagnation line free stream conditions of the plasma flow, 20 mm in front of the probe.**

Parameter	Value
Velocity <sup>a</sup> / m/s [40]	3350
Density <sup>b</sup> / kg/m <sup>3</sup>	$2.3642 \times 10^{-4}$
Pressure <sup>a</sup> / kPa [30]	1660
Translational temperature <sup>a</sup> / K [40]	11780
Vibrational temperature <sup>a</sup> / K [30]	13280
Rotational temperature <sup>a</sup> / K [30]	11660
Electronic temperature <sup>a</sup> / K [30]	8440
Mole fraction N <sub>2</sub> <sup>b</sup>	$1.8094 \times 10^{-5}$
Mole fraction O <sub>2</sub> <sup>b</sup>	$1.3192 \times 10^{-8}$
Mole fraction NO <sup>b</sup>	$6.8895 \times 10^{-7}$
Mole fraction N <sup>b</sup>	$5.0226 \times 10^{-1}$
Mole fraction O <sup>b</sup>	$1.4673 \times 10^{-1}$
Mole fraction N <sub>2</sub> <sup>+</sup> <sup>b</sup>	$3.6373 \times 10^{-6}$
Mole fraction O <sub>2</sub> <sup>+</sup> <sup>b</sup>	$2.5343 \times 10^{-8}$
Mole fraction NO <sup>+</sup> <sup>b</sup>	$6.9526 \times 10^{-6}$
Mole fraction N <sup>+</sup> <sup>b</sup>	$1.4572 \times 10^{-1}$
Mole fraction O <sup>+</sup> <sup>b</sup>	$2.7378 \times 10^{-2}$
Mole fraction e <sup>-</sup> <sup>b</sup>	$1.7386 \times 10^{-1}$

<sup>a</sup> Measurement<sup>b</sup> Enthalpy and static pressure equilibrium computation**Table 2 Material properties and measured stagnation point conditions of the samples.**

Parameter	CALCARB	ASTERM
Carbon mass fraction [38]	1.0	0.7
Phenolic mass fraction [38]	0.0	0.3
Material density / kg/m <sup>3</sup> [38, 41]	180	350
Surface temperature / K [41]	3025	2780
Recession rate / $\mu\text{m/s}$ [41, 42]	55	32

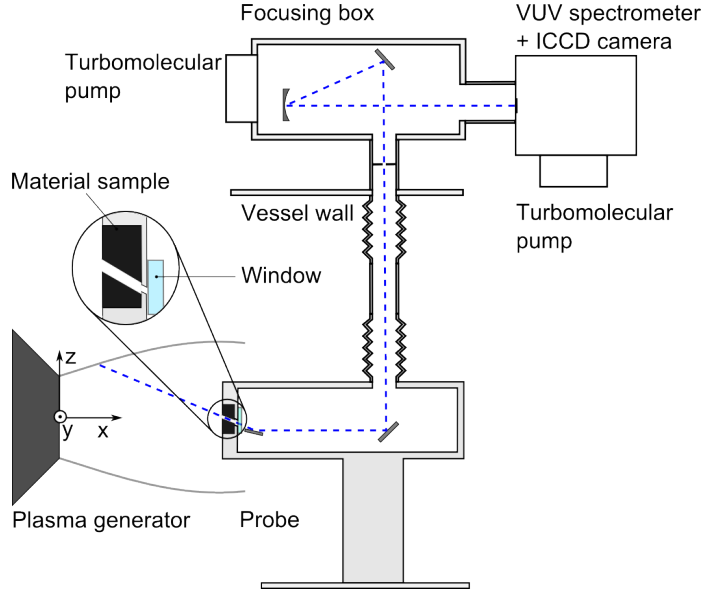


**Fig. 2 Setup of the VUV spectroscopic system. Optical path as dashed [47].**

1 m focal length spectrometer coupled with an ANDOR iStar 340T intensified charge-coupled device (ICCD) camera is used. The spectral resolution of the setup is 0.01 nm/px with an instrumental broadening of  $\delta_{\text{Gauss}} = 0.06$  nm and  $\delta_{\text{Lorentz}} = 0.02$  nm full width at half maximum (FWHM). An absolute calibration for radiance of the VUV system is conducted using a MCPHERSON 632 deuterium lamp. A detailed description of the setup can be found in [30].

It has been noticed during the test campaign that the ASTERM material samples caused a contamination of the window. Phenolic resin from the material samples generates a thin coating on the window surface. Transient measurements during the experiment, i. e. when the sample is in the flow, showed no further change in signal strength for the remainder of the test time. It is therefore believed that the degree of contamination does not increase during the experiment and that the contamination is generated during the start up phase of the generator. During that time, the sample is situated outside the plasma jet, however, a slight pre-heating is observed. In order to account for the contamination, a post-test calibration is conducted for each test with the contaminated window in place. The CALCARB samples also exhibited a contamination effect. After each experiment the window was coated with a layer of particles obviously originating from the material sample. Transient measurements during an experiment showed that after a time of 3–4 seconds the measured signal strength decreases gradually over the test time until the optical path is

completely blocked by the contamination layer. Thus, it is believed that the contamination starts when the sample is introduced into the flow and grows steadily over the duration of the experiment. In order to account for this, a pre-test calibration is used for each test and only the data collected immediately after the sample is positioned into the flow is considered for further analysis.

### C. UV/VIS spectroscopy

The UV/VIS spectroscopy, covering the 300 nm–810 nm wavelength range, has been setup on the side of the vacuum chamber. The plasma in front of the material samples has been investigated using a classical experimental setup as it has been applied by other researchers at IRS [32, 34, 36]. Measurements are taken with a PRINCETON INSTRUMENTS SpectraPro 2758 spectrometer coupled with an ANDOR DU920N-OE camera. A vertically orientated rectangular region, 60 mm high and 1.6 mm (FWHM) wide, at approximately 5 mm in front of the probe surface is imaged. The setup is depicted schematically in Fig. 3. The spectral resolution of the setup is 0.12 nm/px with an instrumental broadening of  $\delta_{\text{Gauss}} = 0.24$  nm and  $\delta_{\text{Lorentz}} = 0.12$  nm FWHM while each acquisition covers a spectral range of 120 nm [30]. All acquisitions presented in this study are acquired at 25 s after the probe has been exposed to the plasma flow. In post-processing the different acquisitions are concatenated to the full spectrum ranging from 300 nm to 810 nm. The UV/VIS system is calibrated using a GIGAHERTZ-OPTIK BN0102 integrating sphere for absolute radiance. The calibrated measurements are processed using an Abel transform in order to obtain the local emission coefficient using the algorithm developed by Fulge et al. [48].

## III. Results

### A. Stagnation point spectra

In this section the resulting calibrated stagnation point spectra for the three different materials are presented. **The radiating species are identified and the influence of the different material samples on the emitted radiation is quantified.** Figure 4 shows the VUV stagnation point spectra. Some spectral intervals have not been measured due to low signal strength or oversaturation and are indicated accordingly. The carbon multiplets at 156 nm and 165 nm of the CALCARB spectrum are not calibrated because of window contamination. However, it was possible



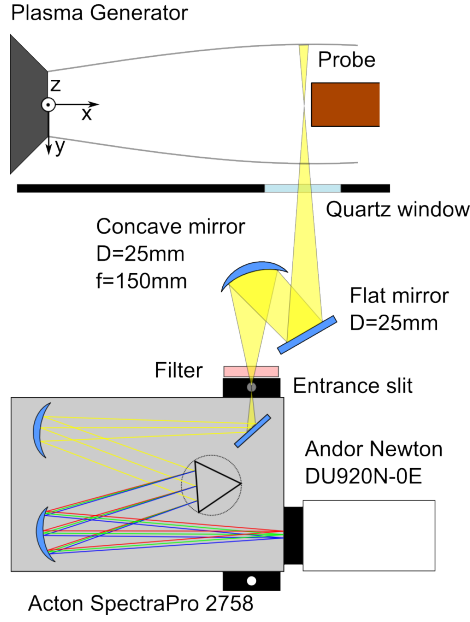


**Fig. 3 Setup of the UV/VIS spectroscopic system [30].**

to estimate the line intensity based on other spectral features. The analysis of the self-absorption of atomic carbon (see section III C) revealed that most of the lines are black body limited including the multiplets at 165 nm and 156 nm. The measured population densities (shown in section III C) confirm that the peak spectral radiance of these multiplets is black body limited by the same black body limiting curve that applies to several of the carbon multiplets at 127 nm [49]. This black body curve is calculated based on the peak spectral radiance of the multiplets at 127 nm. The intensity of the multiplets at 165 nm and 156 nm is estimated by scaling them such that their peak spectral radiance corresponds to this black body curve.

All spectra are corrected for absorption by molecular oxygen inside the bore hole between the stagnation point and the window applying the methodology presented in Ref. [30]. Here, the measured radiance of black body limited atomic lines is used to assess the amount of absorption by molecular oxygen in the bore hole. For the ASTERM material sample it is not possible to deduce the amount of absorption in the bore hole since the atomic lines are possibly not black body limited. It is assumed that the amount of absorption in the bore hole is equal to the absorption measured during the CALCARB tests.

Atomic nitrogen and oxygen lines dominate the VUV radiance for all materials. The atomic

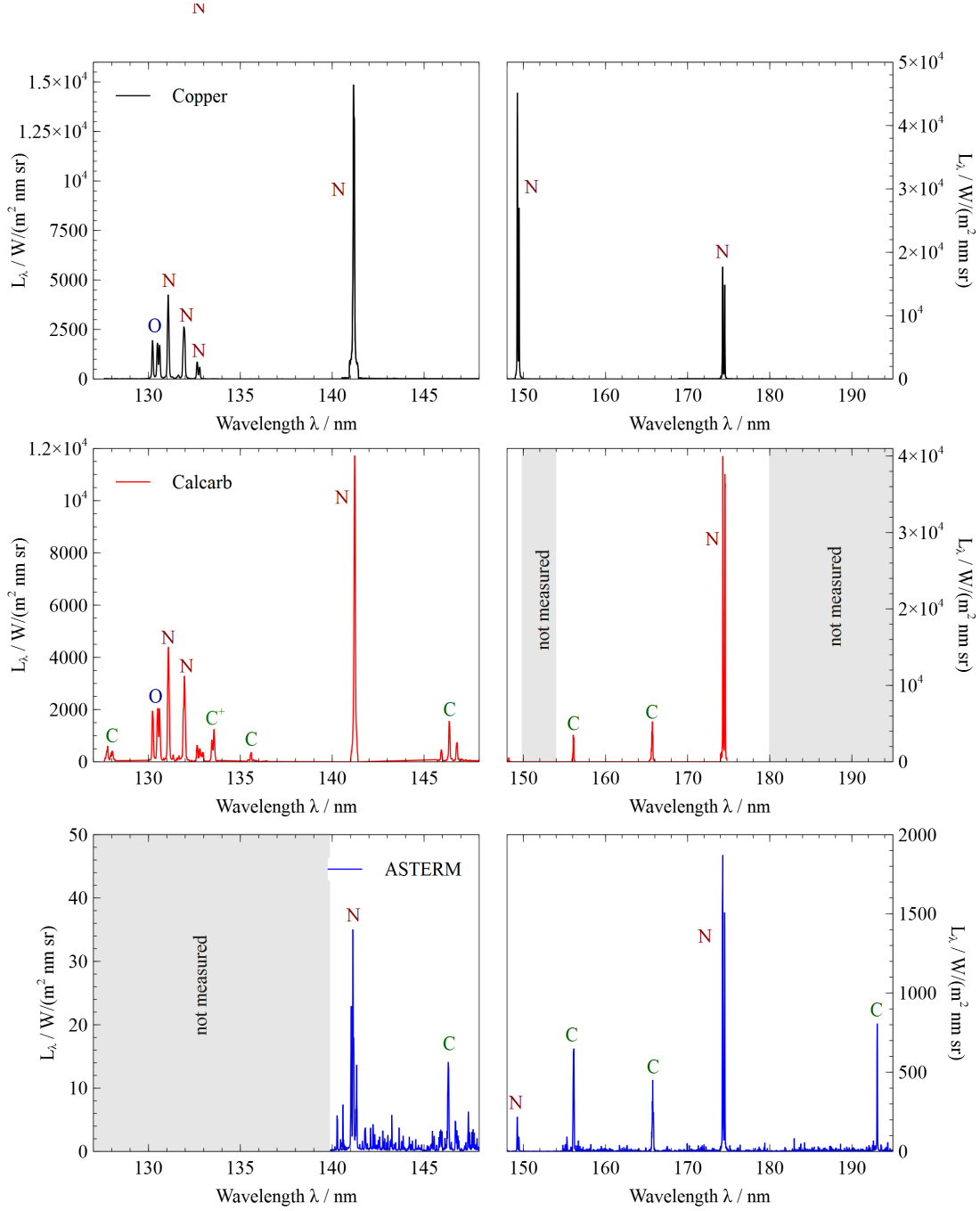


**Fig. 4 Stagnation point VUV spectrum for ASTERM, CALCARB and copper.**

oxygen and nitrogen multiplets in front of CALCARB and copper are of equal intensity, except for the 174nm nitrogen multiplet, which is stronger in front of CALCARB. The carbon (neutral and singly ionized) lines in the spectrum in front of the CALCARB sample add a significant amount to the total radiance which is 1.81 times stronger compared to the non-ablating copper. The nitrogen lines in front of ASTERM are much weaker than in front of copper. The total radiance in front

of ASTERM in the measured wavelength interval is 14.8 times weaker than in front of copper. For a direct comparison between the two ablative materials, the integral radiance of individual atomic multiplets is considered. The nitrogen 174 nm multiplet radiance incident on CALCARB is 21.2 times stronger than in the case of ASTERM, while the 165 nm carbon multiplet is 12 times stronger. Concluding, all atomic multiplets are significantly weaker in the ASTERM spectrum, while the multiplets in the CALCARB spectrum are even stronger than in the case of the copper reference material. The phenolic matrix of ASTERM exhibits a strong influence on the VUV radiance and reduces nitrogen atomic radiation by a factor of over 20. The approximate radiative heat flux of various wavelength intervals is obtained by multiplying the measured radiance by  $2\pi$  [15]. The resulting values are summarized in Table 3.

Figure 5 shows the local emission coefficient in the UV/VIS interval in front of CALCARB, ASTERM, and copper for a point 5 mm in front of the probe on the stagnation streamline at 25 s after the probe has been first exposed to the plasma. The spectral region is dominated by molecular emission of  $N_2^+$  for all materials. Only in front of the copper and the CALCARB sample is  $N_2$  radiation detected. In front of the CALCARB and the ASTERM sample, strongly radiating CN appears. Atomic lines of nitrogen and oxygen are similar in magnitude for copper and ASTERM samples. The atomic lines in front of CALCARB are significantly stronger. In the respective wavelength intervals that have been measured for the material samples, the integrated emission coefficient for CALCARB is 4.1 times stronger than for copper. For ASTERM, it is 1.23 times stronger than for copper. Comparing the carbon based material samples directly in the wavelength range 320 nm–575 nm, the wavelength integrated emission coefficient in front of CALCARB is 2.8 times stronger than in front of ASTERM. The measured values of the wavelength integrated emission coefficient are summarized in Table 3.

## **B. Radial distribution of excitation temperatures and excited species**

This section presents results obtained from an analysis of the local emission spectra in the UV/VIS spectral region.

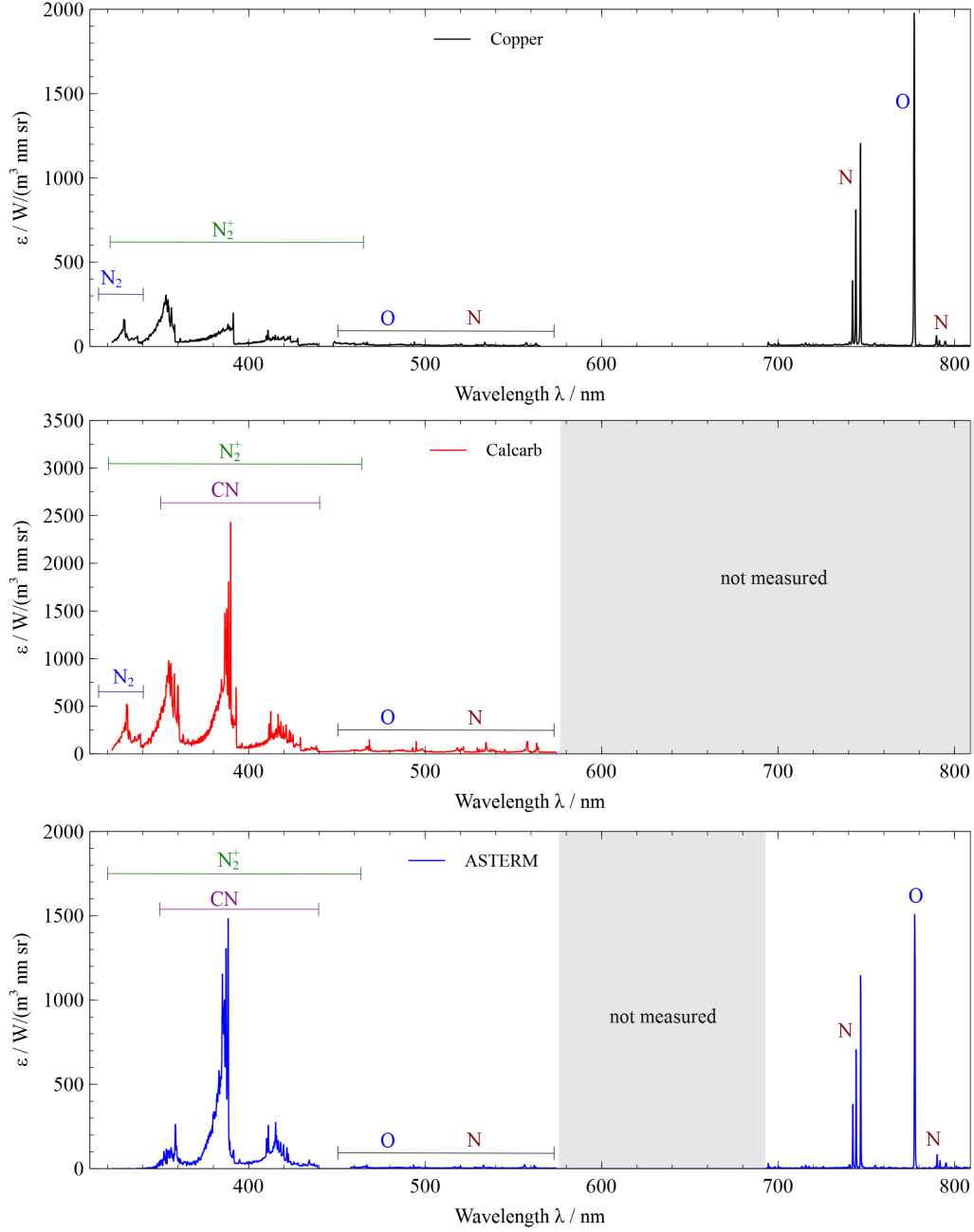


Fig. 5 UV/VIS spectrum on the stagnation streamline 5 mm in front of the probe surface.

#### 1. Molecular radiation

The molecular radiation is used to quantify the coupling between ablation and the thermochemical state of the boundary layer. This section provides the spatial distribution of different excited molecules and their respective excitation temperatures.

**Table 3 Radiative heat flux ( $\dot{q}$ ) and wavelength integrated emission coefficient ( $\varepsilon_c$ ) measurements.**

Parameter	Wavelength range / nm		Copper	CALCARB	ASTERM
$\dot{q}$ / kW/m <sup>2</sup>	126 nm-180 nm	excluding	40.0	72.4	-
	149 nm multiplet				
$\dot{q}$ / kW/m <sup>2</sup>	140 nm-197 nm		75.1	-	5.1
$\dot{q}$ / kW/m <sup>2</sup>	carbon multiplet	165 nm-	-	5.3	0.4
	167 nm				
$\dot{q}$ / kW/m <sup>2</sup>	nitrogen multiplet	174 nm-	16.9	39.9	1.9
	175 nm				
$\varepsilon_c$ / W/(m <sup>3</sup> sr)	320 nm-575 nm		7770	31910	11440
$\varepsilon_c$ / W/(m <sup>3</sup> sr)	320 nm-810 nm	excluding	11060	-	13560
	575 nm-690 nm				

To deduce radially resolved rotational and vibrational excitation temperatures, simulated spectra are fitted to the measured local emission coefficient of N<sub>2</sub>, N<sub>2</sub><sup>+</sup> and CN in the wavelength range 320 nm-440 nm [32, 34]. The emission is simulated using the radiation database PARADE and requires the input parameters rotational temperature, vibrational temperature and relative species number densities [1, 50]. These parameters are varied until the best match between measurement and simulation is obtained. The resulting simulated spectrum provides the contribution of each molecular species' radiation to the total radiation in the investigated wavelength range. Details of the procedure can be found in [30].

Figure 6 shows the resulting radial distribution of the integrated emission coefficient for the wavelength range 320 nm-440 nm, divided into the contributions from each molecular species. The material sample holder design is a flush mounted sample of 40 mm in diameter inside an 80 mm water-cooled copper housing (see Fig.1). The end of the sample and the probe is indicated in the figures. The biggest contributors are N<sub>2</sub><sup>+</sup> and CN. The N<sub>2</sub><sup>+</sup> distribution in front of CALCARB declines more steeply towards the probe edge than in front of copper and is stronger on the center

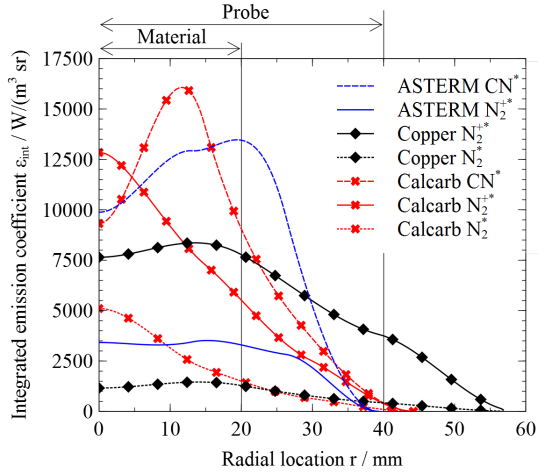


**Fig. 6** Radial distribution of molecular emission 5 mm in front of the probe surface ( $r = 0$  corresponds to the location of the bore hole).

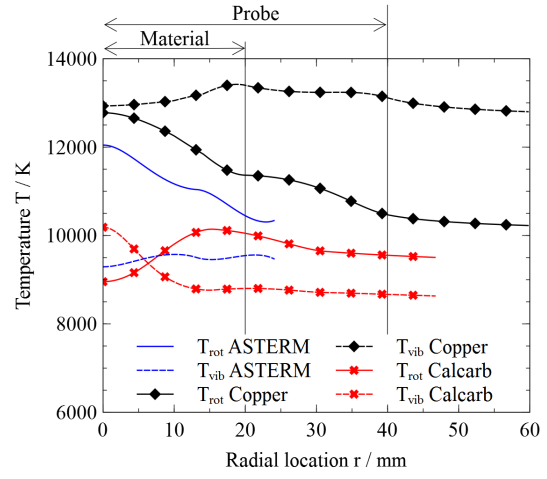


**Fig. 7** Radial distribution of molecular internal temperatures 5 mm in front of the probe surface ( $r = 0$  corresponds to the location of the bore hole).

line. The qualitative  $N_2^+$  distribution in front of ASTERM is similar as in front of copper, but at significantly lower magnitude. The  $N_2$  distribution of CALCARB follows the trend of  $N_2^+$  and is significantly larger in magnitude than in front of copper. In front of both ASTERM and CALCARB, the CN distribution peaks near the edge of the material and declines towards the centerline as well as towards the probe edge. One reason for this behaviour might be the radial distribution of enthalpy. The enthalpy is highest in the center and decreases steadily towards the outside of the flow. This large centerline enthalpy leads to a higher dissociation degree of molecules. As CN exhibits a significantly lower dissociation energy than  $N_2$  or  $N_2^+$  it is dissociated more easily than the nitrogen (neutral and ionized) molecules [51]. This explains why  $N_2$  and  $N_2^+$  radiation peaks in the center while CN radiation decreases towards the center. As the investigated molecular radiation originates from electronically excited states, the distribution might not represent the respective total molecular number density distribution. The electron density is highest in the center which leads to an efficient electronic excitation resulting in a larger amount of radiating molecules.

In Fig. 7 the radial distribution of molecular internal temperatures for the three different materials are presented. Temperatures are presented at locations where the emission coefficient features a sufficient signal to noise ratio. The rotational and vibrational temperatures in front of the copper

sample are highest. Both carbon based materials result in a significant reduction of the molecular temperatures. In front of CALCARB the vibrational temperature increases towards the center while the rotational temperature decreases. Here, the vibrational temperature exhibits the opposite behaviour as is observed in front of copper. The vibrational temperature in front of ASTERM is comparable in magnitude to the values in front of CALCARB but stays rather constant along the radial direction. The decreased vibrational temperature in front of the carbon based materials could be a result of molecules originating from the material. These molecular species, such as CN or C<sub>2</sub> are released at the surface with approximately the surface temperature, i. e. at a lower temperature than the air plasma [52]. The dissociation due to high vibrational excitation is a result of the boundary layer gas chemistry and results in a lowering of the boundary layer enthalpy [9, 53, 54]. The rotational temperature in front of ASTERM, however, almost reaches the values as measured in front of copper and follows the same declining trend towards the probe edge as is observed in front of copper.

## 2. Atomic radiation

**In this section, the coupling between atomic properties and the different materials is investigated. Therefore, the atomic electronic excitation temperature and the particle density of excited states are presented.** Atomic lines in the 450–650 nm range have been investigated. Figure 8 shows the radial distribution of the normalized population density of excited states of atomic nitrogen ( $E_i = 112909.9 \text{ cm}^{-1}$ ,  $\lambda_0 = 574.71 \text{ nm}$ ), oxygen ( $E_i = 106751.5 \text{ cm}^{-1}$ ,  $\lambda_0 = 496.96 \text{ nm}$ ) and carbon ( $E_i = 88568.0 \text{ cm}^{-1}$ ,  $\lambda_0 = 581.63 \text{ nm}$ ). The integrated emission coefficient of atomic multiplets with the respective upper energy states and indicated wavelengths are used to obtain these distributions. The plot is normalized for each species. In front of CALCARB, the distribution of all three atomic species is virtually identical. Similar to the distribution of N<sub>2</sub><sup>+</sup>, the population density declines more steeply towards the probe edge compared to the distribution in front of the copper case. The magnitude of the excited atomic population density in front of CALCARB is far larger than in front of copper. The atomic distribution in front of ASTERM behaves similarly to the values in front of CALCARB as all three species are similarly distributed.

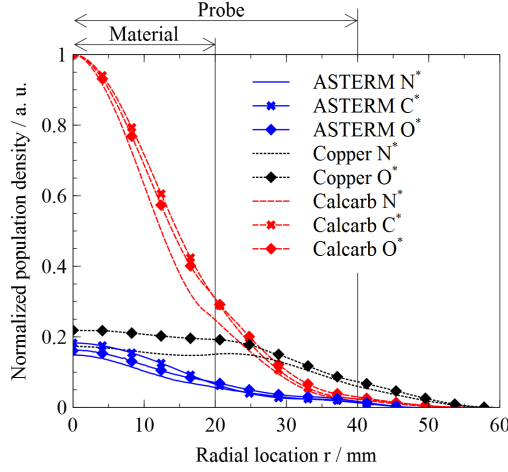


**Fig. 8** Radial distribution of excited atoms 5 mm in front of the probe surface ( $r = 0$  corresponds to the location of the bore hole).

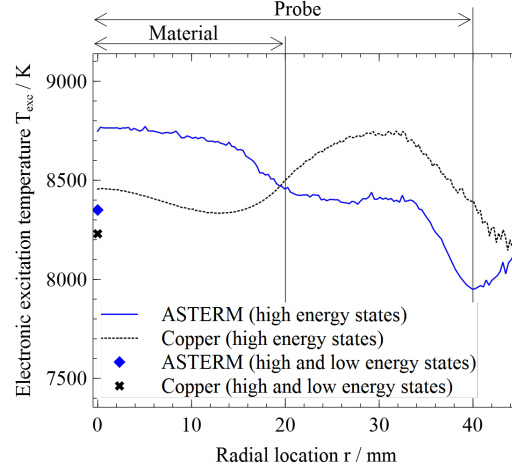


**Fig. 9** Radial distribution of the electronic excitation temperature (N) 5 mm in front of the probe surface ( $r = 0$  corresponds to the location of the bore hole).

However, the magnitude is slightly lower compared to the values in front of the copper sample.

The radial distribution of the electronic excitation temperatures of atomic nitrogen is deduced using the Boltzmann plot method on the UV/VIS spectroscopic data. The emission coefficient of atomic multiplets is spectrally integrated allowing the determination of the local population densities of highly excited energy states [55]. The relative population densities of different states are used to determine the electronic excitation temperature [30–33]. The multiplets used are compiled in Table 5 in Appendix A. Temperatures are obtained at locations where the atomic emission coefficient is clearly separable from underlying molecular radiation. Additionally, temperatures on the centerline are presented which require analysis of the low and high energy states, this is detailed in section III C.

Figure 9 shows the measured electronic excitation temperature in front of copper and ASTERM. In the case of CALCARB not enough multiplets were measured to provide meaningful data. In front of ASTERM a clear separation between the sample material and the probe area can be identified. The temperature reaches a value of about 8800 K in the center and decreases towards the material edge, where it reaches a plateau value of 8400 K in front of the probe housing. At the probe edge the temperature drops to about 8000 K. In front of copper the temperature plateaus at about 8500 K



in the center area of the probe and peaks at about 8800 K at a radial location of approximately 30 mm. The reason of this peak is yet unknown. In contrast to the differences in rotational and vibrational temperatures between the materials, the difference in electronic excitation temperature is almost negligible. In fact, the uncertainty of the measurement is considered to be larger than the temperature discrepancy between the materials.

### C. Excitation temperatures and number densities on the stagnation streamline

This section presents results obtained by coupling the VUV and the UV/VIS spectra. **The ablation flowfield coupling is investigated through the determination of absolute number densities of several radiating species. Furthermore, the thermochemical state of the stagnation line 5 mm in front of the surface is used to quantify the influence of ablation effects on species densities and excitation temperatures.** The analysis of the branching ratio, i. e. the characteristic shape of self-absorbed multiplets in the measured VUV spectra, is used to determine number densities of various low energy states including ground states of the three atomic species (N, O, C) [56]. The multiplets considered are compiled in Tables 6 and 7 in Appendix A. The number densities are calculated by fitting a simulation to the measured data using the following procedure. A one-dimensional radiative transport calculation of each atomic multiplet along the line of sight of the VUV spectroscopic system is conducted. It is assumed that the spatial distribution of low energy states along this line of sight corresponds to the measured distribution of highly excited atomic states [30]. The lineshape along the line of sight is calculated using Doppler and Stark broadening. The required translational temperature is assumed to be equal to the measured rotational temperature (see section III B) [54]. Stark broadening is calculated using the data provided by Johnston et al., using the measured electronic excitation temperature (see section III B) and an equilibrium electron density of  $2.9 \times 10^{21} \text{ m}^{-3}$  [57]. Subsequently, the calculated spectrum is convolved with the instrument slit function and compared to the measured spectrum. In this procedure, the lower state population density is a variable input parameter which is varied, i. e. the spatial distribution of the lower state is scaled, until the best agreement between the calculated and the measured spectra is obtained. Further details of the methodology can be found in [30].

The resulting population densities are applied in a Boltzmann plot corresponding to the stag-

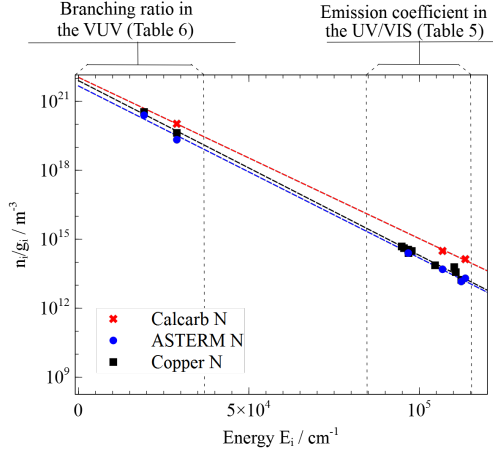


**Fig. 10 Boltzmann plot (N) on the stagnation streamline 5 mm in front of the probe surface.**

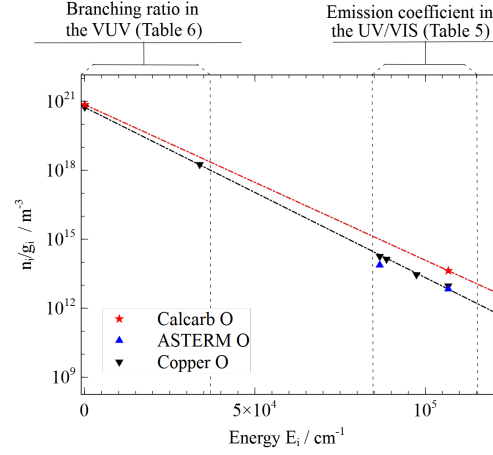


**Fig. 11 Boltzmann plot (O) on the stagnation streamline 5 mm in front of the probe surface.**

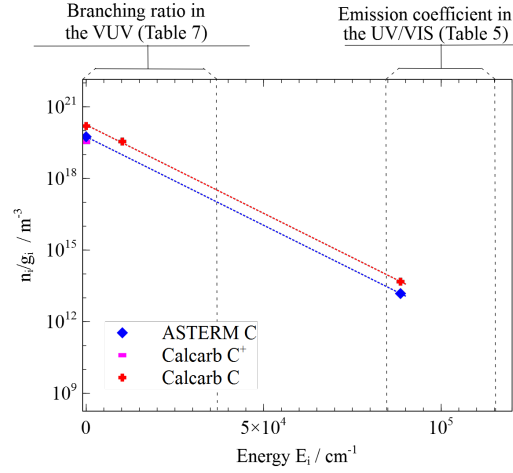


**Fig. 12 Boltzmann plot (C) on the stagnation streamline 5 mm in front of the probe surface.**

nation point region approximately 5 mm in front of the probe surface (see Figs 10 to 12). The figures contain low energy states obtained by analyzing the branching ratio of the multiplets in the VUV regime as well as high energy states obtained from UV/VIS spectroscopy from the side (see section III B). The ground states of oxygen, carbon and singly ionized carbon have been measured, however, the ground state of nitrogen was inaccessible in front of CALCARB and ASTERM. All energy states measured exhibit a Boltzmann distribution which is indicated by a linear correlation function. In front of ASTERM it is not possible to obtain the oxygen ground state and the oxygen high energy data is based on very weak multiplets which are overlapped by molecular bands adding

too high uncertainty to the absolute population density of those states. This data is not further analyzed. The Boltzmann plots are used to obtain electronic excitation temperatures for the different species (see Fig. 9) [31].

In the cases where the ground state is accessible it is possible to sum over all energy states and thus obtain an absolute atom number density. Energy states which have not been measured directly have been interpolated using the Boltzmann relation which is assumed to be reasonable as all lower states measured obey a Boltzmann distribution and equilibration with free electrons is faster for high energy states [58]. The nitrogen ground state is extrapolated from the respective Boltzmann distribution. This extrapolation only allows for a qualitative comparison between the different materials. Additionally, the molecular radiation is used to obtain extrapolated number densities. The known rotational and vibrational temperatures and the known absolute emission coefficient obtained from the molecular spectra are used. Furthermore, assuming a Boltzmann distribution of the electronic states with the electronic excitation temperature taken from the atomic Boltzmann plot (Fig. 10), absolute number densities are obtained by matching the absolute emission coefficient of the measurement with a PARADE simulation [59]. As in the case of atomic nitrogen, this procedure is an extrapolation to low energy and ground states and can therefore only provide qualitative information to be used for a comparison between materials. Additionally, rotational and vibrational temperatures of CN of the actual re-entry flight measured during an observation campaign with the ultraviolet spectrograph AUS are presented [60]. These temperatures are of phenomenological nature as all the radiating plasma in front of the vehicle was measured. However, the spectra are highly dominated by CN which radiates mostly in the boundary layer close to the surface. Therefore, the measured temperatures are attributed to the boundary layer radiation [6, 9]. The respective data is presented in Table 4.

The electronic excitation temperatures of nitrogen and oxygen are both approximately 700 K higher in front of CALCARB compared to copper. In front of ASTERM the nitrogen electronic excitation temperature increases by only 130 K compared to the copper case. The electronic excitation temperatures of atomic carbon in front of CALCARB and ASTERM are identical. Generally, the electronic excitation temperature is weakly affected by the use of different material samples

**Table 4 Flow properties on the stagnation streamline 5 mm in front of the probe surface.**

	Copper	CALCARB	ASTERM	Flight [60]
$T_{\text{rot}} / \text{K}$	12780	8950	12050	13000
$T_{\text{vib}} / \text{K}$	12930	10190	9290	11500
$T_{\text{exc,N}} / \text{K}$	8230	8910	8350	-
$T_{\text{exc,O}} / \text{K}$	8430	9230	-	-
$T_{\text{exc,C}} / \text{K}$	-	8430	8430	-
$n_{\text{N}} / \text{m}^{-3}$	$3.5 \times 10^{22}$	$4.9 \times 10^{22}$	$2.1 \times 10^{22}$	-
$n_{\text{O}} / \text{m}^{-3}$	$6.5 \times 10^{21}$	$8.7 \times 10^{21}$	-	-
$n_{\text{C}} / \text{m}^{-3}$	-	$1.7 \times 10^{21}$	$5.5 \times 10^{20}$	-
$n_{\text{C}^+} / \text{m}^{-3}$	-	$2.0 \times 10^{20}$	-	-
$n_{\text{N}_2} / \text{m}^{-3}$	$1.5 \times 10^{21}$	$1.6 \times 10^{21}$	-	-
$n_{\text{N}_2^+} / \text{m}^{-3}$	$1.9 \times 10^{18}$	$2.3 \times 10^{18}$	$8.0 \times 10^{17}$	-
$n_{\text{CN}} / \text{m}^{-3}$	-	$1.6 \times 10^{18}$	$2.2 \times 10^{18}$	-

(between 1 % and 9 % compared to copper). The rotational and vibrational temperatures are much more affected. Compared to copper the vibrational temperature is decreased significantly by the use of a carbon based material sample (between -21 % and -28 %). The rotational temperature is lowest for CALCARB and comparable in magnitude in front of ASTERM and copper (between -6 % and -30 % compared to copper). The flight data shows temperatures close to those obtained in the plasma wind tunnel, indicating that the boundary layer reconstruction in the ground based facility works as intended. Nevertheless, no further quantitative comparison is attempted as the flight data is a somewhat averaged value of the whole flowfield while the values in the plasma wind tunnel are local flow properties.

The atomic densities of all species considered are largest in front of CALCARB and lowest in front of ASTERM (between -40 % and 40 % compared to copper and over a factor of 2 between the ablative materials). This is in accordance to Fig. 4 where the VUV absolute atomic radiance also

follows this trend. As expected, the blowing effect encountered in the case of the ASTERM samples decreases the boundary layer enthalpy by injecting cold gas into the flow [53]. The lower enthalpy results in a lower atom number density in the boundary layer. The high surface catalycity of copper is the reason for the lower atom density compared to CALCARB.

The extrapolated molecular number densities of  $N_2$  and  $N_2^+$  in front of copper and CALCARB are similar while the  $N_2^+$  number density in front of ASTERM is significantly smaller and the  $N_2$  number density is too low for a detectable signal in the emission spectrum. However, in front of ASTERM more CN molecules are measured when compared to CALCARB. Hence, the additional pyrolysis gas and possible spalled particles of ASTERM samples are a source of carbonaceous species which undergo further reactions to form CN [61].

Generally, it is noticed that the number density in front of CALCARB is highest for almost all measured species. This phenomenon could be the result of a comparably low translational temperature. Considering that the rotational and translational temperature relax very quickly with each other, the rotational temperature in front of CALCARB can be used as a measure of the translational temperature [54]. A lower translational temperature increases the number density in the flow which explains the trend pointed out before.

#### IV. Conclusion

Experiments aiming to investigate ablation-radiation coupling have been successfully conducted in the plasma wind tunnel PWK1. Optical emission spectroscopic measurement systems for different wavelength intervals have been setup to investigate the radiation of the hot flow in front of cooled copper, a carbon preform (CALCARB) and a commercial carbon phenolic ablator (ASTERM). VUV radiation is measured through a bore hole in the stagnation point while radiation in the UV/VIS regime is measured viewing the plasma from the side. The analysis of the data in the UV/VIS results in a local distribution of the emission coefficient of the species of interest, while the VUV measurements provide the stagnation point spectral radiance.

The VUV radiation incident on the stagnation point is strongest in front of CALCARB and over a magnitude lower in front of ASTERM. It is concluded that through the decomposition of the phenolic matrix of ASTERM samples, atomic nitrogen emission is reduced by a factor of 21.2. This

clearly shows the blockage effect of the pyrolysis gas. However, for both carbon based materials atomic lines of carbon originating from the samples add a significant fraction to the total measured radiance.

Molecular radiation is weakest in front of copper and radiation in front of CALCARB is 2.8 times stronger than in front of ASTERM. Excitation temperatures of molecules and atoms have been measured. Both carbon based material samples lead to a decrease in the vibrational temperature while the rotational temperature is also decreased in front of CALCARB. The electronic excitation temperature shows a slight increase in front of the surface of a CALCARB material sample.

From the measurements presented in this study, a clear influence of ablation on the measured radiation is shown. In front of a purely carbonaceous material without phenolic resin the radiative heating to the surface is increased in the VUV and the UV/VIS spectral regions. The introduction of a phenolic matrix reduces the VUV radiation to the surface significantly and cools the plasma in front of the material sample. Excitation temperatures are up to 30 % lower and atomic number densities are by over a factor of 2 lower. Consequently, a significantly lower radiative heat flux is measured. From the measurements, lightweight carbon phenolic ablators are considered to mainly reduce the radiative heat load by pyrolysis.

### Acknowledgement

The authors gratefully acknowledge the financial support by ESA through the research grant No. 2011/ITT-6632/PL. The dedicated support of the institute's workshop is indispensable and gratefully acknowledged. The authors would like to thank the project partners for sharing their hardware and knowledge and the colleagues from the High Enthalpy Flow Diagnostics Group for the continuous and prompt help. Additionally, the authors would like to acknowledge the input of the reviewers whose comments and suggestions increased the quality of the paper significantly.

### References

- [1] Liebhart, H., Herdrich, G., and Merrifield, J. A., "Advances for Radiation Modeling for Earth Re-entry in PARADE: Application to the STARDUST Atmospheric Entry," *43rd AIAA Thermophysics Conference*, AIAA, 2012.

- [2] Grinstead, J. H., Jenniskens, P., Cassell, A., Albers, J., and Winter, M. W., “Airborne Observation of the Hayabusa Sample Return Capsule Re-entry,” *42nd AIAA Thermophysics Conference*, AIAA, 2011.
- [3] Gnoffo, P. A., “Planetary-Entry Gas Dynamics,” *Annual Review of Fluid Mechanics*, Vol. 31, 1999, pp. 459–494.
- [4] Brandis, A. M. and Johnston, C. O., “Characterization of Stagnation-Point Heat Flux for Earth Entry,” *45th AIAA Plasmadynamics and Lasers Conference*, Atlanta, GA, June 2014.
- [5] Anderson, J. D., *Hypersonic and High-Temperature Gas Dynamics, 2nd Edition*, AIAA Education Series, 2nd ed., 2006.
- [6] Gupta, R. N., “Aerothermodynamic Analysis of Stardust Sample Return Capsule with Coupled Radiation and Ablation,” *Journal of Spacecraft and Rockets*, Vol. 37, No. 4, July 2000, pp. 507–514.
- [7] Ried, R. C., Rochelle, W. C., and Milhoan, J. D., “Radiative Heating to the Apollo Command Module: Engineering Prediction and Flight Measurement,” Tech. Rep. NASA-TM-X-58091, Johnson Space Center, April 1972.
- [8] Hoshizaki, H. and Lasher, L. E., “Convective and Radiative Heat Transfer to an Ablating Body,” *Thermophysics Conference*, No. AIAA-67-327, AIAA, 1967.
- [9] Johnston, C. O., Gnoffo, P. A., and Mazaheri, A., “Influence of Coupled Radiation and Ablation on the Aerothermodynamic Environment of Planetary Entry Vehicles,” *Radiation and Gas-Surface Interaction Phenomena*, Vol. 218 of *RTO Lecture Series*, 2013.
- [10] Na, J., Park, C., Baek, S.-W., and Muylaert, J., *Preliminary Design of Super-Orbital Earth Entry Flight Experiment Using VOLNA Launcher*, Aerospace Sciences Meetings, American Institute of Aeronautics and Astronautics, may 2008, doi:10.2514/6.2008-1129.
- [11] Park, C., “Calculation of Stagnation-Point Heating Rates Associated with Stardust Vehicle,” *AIAA Journal of Spacecrafts and Rockets*, Vol. 44, No. 1, 2007.
- [12] Johnston, C. O., Gnoffo, P. A., and Sutton, K., “Influence of Ablation on Radiative Heating for Earth Entry,” *Journal of Spacecrafts and Rockets*, Vol. 46, 2009, pp. 481–491.
- [13] Johnston, C. O., Mazaheri, A., Gnoffo, P. A., Kleb, B., Sutton, K., Prabhu, D., Brandis, A. M., and Bose, D., “Assessment of Radiative Heating Uncertainty for Hyperbolic Earth Entry,” *42nd AIAA Thermophysics Conference*, June 2011.
- [14] Park, C., “Stagnation-Point Radiation for Apollo 4,” *Journal of Thermophysics and Heat Transfer*, Vol. 18, No. 3, July 2004, pp. 349–357.
- [15] Laux, C. O., Winter, M., Merrifield, J. A., Smith, A., and Tran, P., “Influence of Ablation Products on the Radiation at the Surface of a Blunt Hypersonic Vehicle at 10 km/s,” *41st AIAA Thermophysics*

Conference, No. AIAA 2009-3925, 2009.

- [16] Park, C., Abe, T., and Inatani, Y., “Research on the heatshield for MUSES-C Earth reentry,” *7th AIAA/ASME Joint Thermophysics and Heat Transfer Conference*, AIAA, 1998.
- [17] Cruden, B., Martinez, R., Grinstead, J. H., and Olejniczak, J., “Simultaneous Vacuum Ultraviolet through Near IR Absolute Radiation Measurement with Spatiotemporal Resolution in an Electric Arc Shock Tube,” *41st Thermophysics Conference*, AIAA, 2009.
- [18] McClenahan, J. O., “Vacuum Ultraviolet Line Radiation Measurements of a Shock-Heated Nitrogen Plasma,” Tech. Rep. NASA TN D-6920, Ames Research Center, Moffet Field, California, Aug. 1972.
- [19] Sheikh, U., Morgan, R., Zander, F., Eichman, T., and McIntyre, T., “Vacuum Ultraviolet Emission Spectroscopy System for Superorbital Reentries,” *18th AIAA/3AF International Space Planes and Hypersonic Systems and Technologies Conference*, AIAA, 2012.
- [20] Wood, A. D., Hoshizaki, H., Andrews, J. C., and Wilson, K. H., “Measurements of the Total Radiant Intensity of Air,” *AIAA Journal*, Vol. 7, No. 1, Jan. 1969, pp. 130–139.
- [21] Sutton, K., “Air radiation revisited,” *AIAA 19th Thermophysics Conference*, June 1984.
- [22] Palumbo, G., Craig, R. A., Whiting, E., and Park, C., “Measured Specific Intensity from 130 to 900nm at the Stagnation Point of a Model in an Arcjet Flow of 7.8km/s,” *Journal of Quantitative Spectroscopy and Radiative Transfer*, Vol. 57, No. 2, 1997, pp. 207–236.
- [23] Löhle, S., Brandis, A., Hermann, T., and Peter, J., “Numerical Investigation of the Re-entry Flight of Hayabusa and Comparison to Flight and Ground Testing Data,” *43rd AIAA Thermophysics Conference*, AIAA, New Orleans, LA, 2012.
- [24] Auweter-Kurtz, M., Kurtz, H., and Laure, S., “Plasma Generators for Re-entry Simulation,” *Journal of Propulsion and Power*, Vol. 12, No. 6, November-Dezember 1996, pp. 1053–1061.
- [25] Auweter-Kurtz, M. and Wegmann, T., “Overview of IRS Plasma Wind Tunnel Facilities,” *RTO Educational Notes*, Vol. 8, Oct. 1999.
- [26] Dabalà, P., Hilfer, G., and Auweter-Kurtz, M., “Investigation of the Oxidation Behaviour of Thermal Protection Materials Supported by Mass Spectrometry,” *2nd European Symposium on Aerothermodynamics for Space Vehicles*, Nov. 1994, pp. 237–246.
- [27] Laux, T., Auweter-Kurtz, M., Wegmann, T., Morino, Y., Yoshinaka, T., Park, C., and Speckmann, H. D., “Comparison of Ablation Material Tests in a Plasma Wind Tunnel and Laser Heating Facilities,” *3rd European Workshop on Thermal Protection Systems*, March 1998.
- [28] Löhle, S., Hermann, T., Zander, F., Fulge, H., and Marynowski, T., “Ablation Radiation Coupling Investigation in Earth Re-entry Using Plasma Wind Tunnel Experiments,” *30th Aerodynamic Measurement*



- [29] Loehle, S., Hermann, T., and Zander, F., “Experimental Assessment of the Performance of Ablative Heat Shield Materials from Plasma Wind Tunnel Testing,” *8th ESA Workshop on Thermal Protection Systems and Hot Structures*, ESA, 2016.
- [30] Hermann, T., Zander, F., Fulge, H., Löhle, S., and Fasoulas, S., “Characterization of a Re-entry Plasma Wind Tunnel Flow with Vacuum Ultraviolet to Near Infrared Spectroscopy,” *Journal of Thermophysics and Heat Transfer*, 2015, accepted for publication.
- [31] Fletcher, D. G., “Nonintrusive Diagnostic Strategies for Arcjet Stream Characterization,” *Measurement Techniques for High Enthalpy and Plasma Flows*, VKI, RTO — Research and Technology Organization, Rhode-Saint-Genese, Belgium, 1999.
- [32] Winter, M. W., *Emissionsspektroskopische Untersuchung der Umströmung von Probenkörpern in hochenthalpen Plasmaströmungen*, Ph.D. thesis, Institut für Raumfahrtssysteme, Stuttgart, 2007.
- [33] van der Sijde, B. and van der Mullen, J. A. M., “Temperature Determination in non-LTE Plasmas,” *Journal of Quantitative Spectroscopy and Radiative Transfer*, Vol. 44, No. 1, 1990, pp. 39–46.
- [34] Röck, W. and Auweter-Kurtz, M., “Spectral Measurements in the Boundary Layer of Probes in Nitrogen/Methane Plasma Flows,” *32nd Thermophysics Conference*, Atlanta, GA, June 23-25 1997, AIAA-1997-2525.
- [35] Löhle, S., Wernitz, R., Herdrich, G., Fertig, M., Röser, H.-P., and Ritter, H., “Airborne Re-entry Observation Experiment SLIT: UV Spectroscopy during Stardust and ATV1 Re-entry,” *CEAS Space Journal*, Vol. 1, No. 1, 2010.
- [36] Wernitz, R., Eichhorn, C., Marynowski, T., and Herdrich, G., “Plasma Wind Tunnel Investigation of European Ablators in Nitrogen/Methane Using Emission Spectroscopy,” *Hindawi International Journal of Spectroscopy*, Vol. 2013, 2013.
- [37] Helber, B., Chazot, O., Magin, T., and Hubin, A., “Ablation of carbon preform in the VKI Plasmatron,” *43rd Thermophysics Conference*, No. AIAA 2012-2876, AIAA, 2012.
- [38] MacDonald, M. E., Jacobs, C., Laux, C. O., Zander, F., and Morgan, R., “Measurements of Air Plasma/Ablator Interactions in an Inductively Coupled Plasma Torch,” *Journal of Thermophysics and Heat transfer*, Vol. 29, No. 1, 2015, pp. 12–23.
- [39] Bouilly, J.-M. and Leleu, F., “Ablative Thermal Protections for Planetary Entry: An Overview,” 4th International Symposium on Atmospheric Reentry Vehicles and Systems, Arcachon, 21-25 March 2005.
- [40] Zander, F. and Loehle, S., “Analysis of Air Plasma Flows in Magnetoplasmadynamic Arcjet Testing,” *46th AIAA Thermophysics Conference*, Washington, DC, June 2016.

- [41] Loehle, S., Hermann, T., and Zander, F., “Experimental Assessment of the Performance of Ablative Heat Shield Materials from Plasma Wind Tunnel Testing,” *8th European Workshop on Thermal Protection and Hot Structures*, ESA, 2016.
- [42] Loehle, S., Staebler, T., Reimer, T., and Cefalu, A., “Photogrammetric Surface Analysis of Ablation Processes in High Enthalpy Air Plasma Flow,” *AIAA Journal*, Vol. 53, No. 11, 2015, pp. 3187–3195.
- [43] Kolesnikov, A. F., “Extrapolation from High Enthalpy Tests to Flight Based on the Concept of Local Heat Transfer Simulation,” *Measurement Techniques for High Enthalpy and Plasma Flows*, No. 8B, VKI, RTO — Research and Technology Organization, Rhode-Saint-Genese, Belgium, 1999.
- [44] Loehle, S., Sheikh, U., Hermann, T., McIntyre, T., Leyland, P., Lewis, S., and Wei, H., “Ablation-Radiation Coupling and VUV Radiation Analysis in Expansion Tube and Plasma Wind Tunnel Testing,” *6th International Workshop on Radiation of High Temperature Gases in Atmospheric Entry*, St Andrews, UK, Nov. 2014.
- [45] Loehle, S. and Jenniskens, P., “High Resolution Spectroscopy of the Hayabusa Re-entry using a Fabry-Perot Interferometer,” *Journal of Spacecrafts and Rockets*, Vol. 51, No. 6, Nov. 2014, pp. 1986–1993.
- [46] Gordon, S. and McBride, B. J., “Computer Program for Calculation of Complex Chemical Equilibrium Compositions and Applications,” Reference Publication 1311, NASA, 1996.
- [47] Hermann, T., Zander, F., Fulge, H., Löhle, S., and Fasoulas, S., “Experimental Setup for Vacuum Ultraviolet Spectroscopy for Earth Re-entry Testing,” *30th Aerodynamic Measurement Technology and Ground Testing Conference*, AIAA, 2014.
- [48] Fulge, H., Löhle, S., and Fasoulas, S., “A Noise resistant Abel Transformation Algorithm tested on Optical Emission Spectroscopy,” *Journal of Thermophysics and Heat Transfer*, 2016, accepted.
- [49] Johnston, C. O. and Brandis, A. M., “Features of Afterbody Radiative Heating for Earth Entry,” *11th AIAA/ASME Joint Thermophysics and Heat Transfer Conference*, Atlanta, GA, 2014.
- [50] Smith, A. J., Wood, A., Dubois, J., Fertig, M., Liebhart, H., and Pfeiffer, B., *Plasma Radiation Database PARADE V2.3*, 2009.
- [51] Eichmann, T., *Radiation Measurements in a Simulated Mars Atmosphere*, Ph.D. thesis, University of Queensland, 2012.
- [52] Loehle, S., Hermann, T., Zander, F., and Marynowski, T., “Echelle Spectroscopy for High Enthalpy Flow Diagnostics,” *46th Aerodynamic Measurement Technology and Ground Testing Conference*, AIAA, 2016.
- [53] Turchi, A., Matesanz Saiz, J. J., Magin, T. E., and Chazot, O., “On the Flight Extrapolation of Stagnation-Point Ablative Material Plasma Wind Tunnel Tests,” *8th European Symposium on Aerother-*

*modynamics for Space Vehicles*, 2015.

- [54] Park, C., *Nonequilibrium Hypersonic Aerothermodynamics*, John Wiley & Sons, 1990.
- [55] National Institute of Standards and Technology, <http://physics.nist.gov/PhysRefData/ASD>, 2014.
- [56] Laity, G., *A Radiative Model for Determining Plasma Dissociation Using Vacuum Ultraviolet Self-Absorption Spectroscopy*, Ph.D. thesis, Texas Tech University, May 2013.
- [57] Johnston, C. O., Hollis, B. R., and Sutton, K., “Spectrum Modeling for Air Shock-Layer Radiation at Lunar-Return Conditions,” *Journal of Spacecraft and Rockets*, Vol. 45, No. 5, 2008, pp. 865–878.
- [58] Kunc, J. A. and Soon, W. H., “Collisional-Radiative Nonequilibrium in Partially Ionized Atomic Nitrogen,” *Physical Review A*, Vol. 44, 1989, pp. 5822–5843.
- [59] Löhle, S., Lein, S., Eichhorn, C., Herdrich, G., and Winter, M., “Spectroscopic investigation of an inductively heated CO<sub>2</sub> plasma for Mars entry simulation,” *Journal of Technical Physics*, Vol. 50, No. 3, 2009, pp. 151–164.
- [60] Kraetzig, B., Löhle, S., and Buttsworth, D., “Evolution of Plasma Species and Heat-Shield Temperatures from Hayabusa Reentry Observation,” *AIAA Journal of Spacecrafts and Rockets*, Vol. 51, No. 3, 2014.
- [61] Duffa, G., *Ablative Thermal Protection Systems Modeling*, Aiaa Education Series, The American Institute of Aeronautics and Astronautics, 2013.

## Appendix A

**Table 5** Optically thin atomic multiplets used for the Boltzmann plot method. [55]

$\lambda_0$ / nm	Copper	CALCARB	ASTERM
Nitrogen I			
869.40	✓	×	×
821.41	✓	×	×
745.42	✓	×	✓
939.79	✓	×	×
861.98	✓	×	×
905.24	✓	×	×
648.74	✓	×	×
905.01	✓	×	×
790.67	✓	×	✓
535.02	×	✓	✓
574.71	✓	✓	✓
576.35	✓	×	✓
Oxygen I			
777.55	✓	×	✓
844.88	✓	×	×
926.64	✓	×	×
496.96	✓	✓	✓
Carbon I			
581.63	×	✓	✓

**Table 6** Optically thick atomic multiplets used for the branching ratio analysis (nitrogen and oxygen). [55]

$\lambda_0$ / nm	Copper	CALCARB	ASTERM
Nitrogen I			
120.00	✓	×	×
149.33	✓	×	✓
124.32	✓	×	×
117.69	✓	×	×
117.09	✓	×	×
117.01	✓	×	×
116.80	✓	×	×
116.79	✓	×	×
116.58	✓	×	×
116.41	✓	×	×
174.35	✓	✓	✓
141.19	✓	✓	✓
133.59	✓	✓	×
132.70	✓	✓	×
131.95	✓	✓	×
131.86	✓	✓	×
131.63	✓	✓	×
131.57	✓	✓	×
131.30	✓	✓	×
131.07	✓	✓	×
122.87	✓	×	×
122.52	✓	×	×
119.09	✓	×	×
118.91	✓	×	×
Oxygen I			
130.35	✓	✓	×
121.76	✓	×	×

**Table 7** Optically thick atomic multiplets used for the branching ratio analysis (carbon). [55]

$\lambda_0$ / nm	Copper	CALCARB	ASTERM
Carbon I			
165.72	×	✓	✓
156.11	×	✓	✓
132.93	×	✓	×
128.79	×	✓	×
128.04	×	✓	×
127.98	×	✓	×
127.75	×	✓	×
127.70	×	✓	×
127.41	×	✓	×
127.06	×	✓	×
126.13	×	✓	×
148.18	×	✓	×
147.18	×	✓	×
147.02	×	✓	×
146.81	×	✓	×
146.74	×	✓	×
146.33	×	✓	×
145.90	×	✓	×
136.42	×	✓	×
135.94	×	✓	×
135.93	×	✓	×
135.77	×	✓	×
135.71	×	✓	×
135.58	×	✓	×
135.43	×	✓	×
Carbon II			
133.53	×	✓	×